

MSCI PROJECT
SPAT-TOUMI

IMPERIAL COLLEGE LONDON
DEPARTMENT OF PHYSICS

**Differences in particle sizes and
glaciation temperatures between the
eyewall and periphery clouds of intense
tropical cyclones.**

CID:
01193505

Supervisor:
Ralf Toumi

Assessor:
Arnaud Czaja

Date: December 10, 2020
Word Count: 9534

Abstract

High resolution images from the VIIRS instrument were used to directly observe vertical profiles of temperature T against reflectance ρ in the $3.7\mu\text{m}$ channel, which can be related to the particle effective radius r_e . From these profiles we estimated the glaciation temperature T_g inside the eyewall of a catalogue of 118 tropical cyclones from 2012-2020 using a simplified model of particle size in the mixed-phase and glaciated regions of the eyewall. The distribution of T_g showed a bimodal distribution, with a “cool” peak centered on $236.3 \pm 0.2\text{K}$ and “warm” peak centered on $246.1 \pm 0.8\text{K}$. The presence of the warm peak significantly above the homogeneous freezing temperature indicates the presence of ice forming nuclei. An equal number of cyclones in the catalogue was found in both the warm and cool peaks. In addition the comparison of the composite $T - \rho$ profile between the eyewall and tropical cyclone periphery indicated a consistently lower particle size in the eyewall compared to the periphery. The difference between the eyewall and periphery reflectance inside the rainout region of the clouds were found to have a moderate positive correlation with the maximum wind speed of the TC of 0.535. The gradient of the linear regression was calculated to be $0.222 \pm 0.036\%/kts$. Both these results appear consistent with the presence of sea spray aerosol (SSA) present exclusively to the eyewall of TCs, resulting in smaller droplets in the eyewall.

1 Introduction

Tropical Cyclones (TCs) are the largest storms on Earth and one of the most destructive natural threats bringing wind speeds of over 150mph and a devastating storm surge. In 1970 the Bhola Cyclone is predicted to have killed between 250,000 and 500,000 people[1, 2] making it the deadliest TC ever recorded and in some regions of Bangladesh; the storm killed up to 45% of the local population[2]. Even for highly developed nations such as the United States, TCs can prove incredibly costly with the two largest hurricanes of the 2018 Atlantic season, Florence & Michael, together causing over \$50 million worth of damage to property and infrastructure[3].

Given the threat that TCs post to large portions of the Earth each year, research into TCs is focussed into improving forecasting to allow the impact of these storms to be mitigated. The forecasting of TC is still imperfect, in particular the phenomena of rapid intensification, where TCs can increase its maximum wind speed by 30kts within a 24hr period, is extremely challenging to predict. Current operational models are only able to predict TC rapid intensification with an accuracy from 15-59%.[4]

One reason for this limited accuracy is the issue of factoring in the complex microphysical behaviour within individual clouds into the large macroscopic models. These microphysical processes such as droplet condensation and ice nucleation, are highly sensitive to the exact atmospheric conditions including aerosol composition and concentrations and also able to release large amounts of latent heat which is crucial to TC evolution. Thus by gaining a further understanding on how various aerosols affect the cloud properties inside a TC, it may be possible to gain a deeper understanding of the many stages in a the lifespan of TC which in turn could help save many thousands of lives via more accurate forecasts. The next sections outline the basic principles related to tropical cyclones and cloud microphysics.

1.1 Fundamentals of TCs

Tropical cyclones are warm cored, low pressure weather systems defined as having a sustained wind speed of greater than 33ms^{-1} [5] however TCs with wind speeds up to 96ms^{-1} have been recorded. The exact definition of sustained wind speed can vary between meteorological agencies with the 1 minute sustained speeds commonly used by American agencies and the 10 minute sustained speed used by most others. Like all weather, TCs exist in the atmospheric region called the “troposphere.” This is the lowest region of the atmosphere extending from sea level up to an altitude of up to 18km in the tropics, though the exact height varies with latitude. This upper limit is known as the tropopause and is marked by the presence of a temperature inversion where temperature stops decreasing with increasing altitude. Vertically, TCs extend to cover the entire troposphere whilst horizontally the radius of a TC can vary from 75km to 750km.

The conditions favorable for tropical cyclogenesis were originally identified by Gray[6]. For a TC to form and persist a sea surface temperature (SST) of at least 26°C must be maintained over an ocean depth of at least 5m. TCs also require a non-zero Coriolis parameter, $f = 2\Omega \sin \lambda$, where λ is the latitude and Ω is the Earth rotation frequency. This requirement prevents cyclogenesis within 6° of the equator. The presence of the Coriolis force is needed to maintain the gradient wind balance with the pressure gradient force induced by the low pressure core. This results in the presence of winds that rotate around the core which creates an additional outward component centrifugal force to assist the balance. The direction of rotation is determined by the sign of the Coriolis parameter, in the Northern Hemisphere TCs rotate clockwise and anticlockwise in the Southern Hemisphere. Furthermore, TCs also require a non-local conditional instability; that is that the environmental lapse rate lies between the moist and dry adiabatic lapse rates. This means that an air parcel will resist a vertical displacement until it obtains some critical saturation of moisture. At this stage the parcel will become unstable to a vertical displacement allowing it to quickly rise through the atmosphere. In addition, a low vertical wind shear is desired to prevent “ventilation” where upper level warm air is transported away from the core[7] reducing the concentration of heat making harder for clouds to organize around the core.

Once these conditions have been met, a trigger is required to allow a tropical depression to form. A variety of potential triggers have been found such as disturbances in the African Easterly Jet and pressure waves from the inter-tropic convergence zone. The vast majority of depressions do not go on to form TCs, however occasionally the conditions exist for long enough to allow the maturation of a depression up to a tropical storm and eventually a TC. In the 2019 there were a total of 107 named systems with the West Pacific, East Pacific and North Atlantic basins as the most active respectively accounting for two-thirds of TC activity.

The most identifiable feature of the strongest TCs is the presence of an “eye” containing the low pressure center of the storm. Conditions inside the eye differ to that seen in the rest of the TC with low winds, cool descending air, and little to no cloud present making it easily identifiable. Well defined eyes are typically only seen in the most intense TCs with sustained wind speeds in excess of 58ms^{-1} or those those defined as Category 4 or 5 by the Saffir-Simpson hurricane scale[8].

In contrast, the eyewall which surrounds the eye contains the strongest winds present in the system both horizontally and vertically. The eyewall is a continuous, often symmetric band of deeply convective, cumulonimbus cloud which completely encircles the eye. Inside the eyewall vertical updrafts are typically between $5\text{--}10\text{ms}^{-1}$ [5] but speeds of up to 30ms^{-1} have been measured [9]. The radius of maximum wind (RMW) where the strongest horizontal winds in the TC are measured also is typically located within the eyewall. This region is also responsible for the heaviest amount of precipitation in the entire storm. At the top of the eyewall there is a strong anti-cyclonic outflow mainly comprised of small ice crystals which give rise to the “cloud shield,” a layer of thin cirrus cloud which lies on top of the TC. The development of the eyewall can directly affect the intensity of the entire TC in eyewall replacement cycles. This occurs when a secondary eyewall forms at a greater radial distance than the existing eyewall which then proceeds to deprive the inner eyewall of the moisture needed to sustain itself leading to a short-term de-intensification of the TC. However, the secondary eyewall is able to contract as the primary eyewall disintegrates which from the conservation of angular momentum causes the wind speeds in the new eyewall to speed up, resulting in rapid intensification of the TC. The majority of intense TCs, those greater than category 3, undergo at least one eyewall replacement during their lifespan however as discussed above, predicting such events accurately remains a challenge. The eyewall was the main region of TCs investigated in this project.

Moving further outwards from the eyewall alternating patterns of “moats” and “rainbands” are observed which are needed to form a complete convective cycle. The rainbands are so named as the rising warm, moist air within them is able to result in a considerable amount of precipitation. There are 4 typical configurations of rainbands described by Houze [10]: the principal rainband which extends from TC outer edge into the eyewall in a large spiral, the secondary rainbands which are smaller spirals located near the eyewall, the secondary eyewall which can form in intense TCs and occasionally replace the primary eyewall and the distant rainbands which form at the TC periphery. The clouds in the cyclone periphery were the other region of cloud that was investigated in this project as the inner rainbands are typically obscured by the upper cloud shield. The primary and secondary rainbands often do not exhibit as much convection as the eyewall due to the strong outflow from the eyewall limiting the height of convection. The moats in contrast are regions of dry, cool, descending air which separate the rainbands. Little to no precipitation occurs inside the moats, which makes them easily identifiable on cloud radar.

1.2 Introduction to cloud microphysics

The microphysical process which take place within TCs have a strong effect on TC intensity. Deep convective motion where moisture is transported from the ocean surface up to the tropopause, which results in a large release of latent heat from the condensation and freezing processes is seen in all eyewalls. As air rises it expands and cools adiabatically. This continues until the pressure reaches the saturation vapour pressure where the relative humidity of the parcel is 100%. At this point the air is said to be saturated with respect to water vapour however liquid droplet are not formed instantaneously at this point due to needing to overcome the large energy barrier required to form a spherical droplet. The presence of cloud condensing nuclei (CCN) aerosols provide a surface for the droplets to condense onto. In the absence of CCN, the moist air would be able to obtain supersaturations of up to 40% before

droplet formation whilst CCNs reduce this to under 1%. The atmosphere typically has a high abundance of CCN which can include aerosols from dust, soot and also sea-spray. Condensation is accompanied by a release of latent heat which heats the air allowing continued vertical transport of moisture.

Rosenfeld and Lensky identified 5 distinct regions in the evolution of hydrometeor size in the vertical levels of convective clouds[11]. In this context, hydrometeor refers to any of the possible states that condensed water may exist in, most importantly liquid droplets or ice crystals. When considering particle sizes in the atmosphere the effective radius r_e , is typically used; this is the average radius weighted by cross-sectional area. Hansen and Travis have shown that the effective radius is very close to the mean radius for scattering[12] which allows it to be determined from optical measurements of a cloud such that developed by Nakajima and King[13]. Mathematically, r_e is defined as the ratio of the 3rd and 2nd moments of the particle size distribution $n(r)$:

$$r_e = \frac{\int_0^\infty n(r)r^3 dr}{\int_0^\infty n(r)r^2 dr}. \quad (1)$$

The first stage identified by Rosenfeld & Lensky after droplet formation is a slow diffusional growth region where droplets slowly grow from additional condensation onto existing droplets. Once the droplet radius exceed some critical value, there is a transition to a region where droplets can grow rapidly from collision-coalescence. In the tropics there is generally an abundance of moisture and thus high liquid water content in clouds. This can allow droplets to rapidly grow to such an extent that they can no longer be supported by the updrafts present in the convective cloud causing them to precipitate as warm rain, this occurs above a threshold radius of $14\mu m$ [14]. Warm rain is a relatively rare phenomenon generally only seen in the tropics with the majority of rainfall beginning from ice hydrometeors which form at a much higher altitude. It is well understood that a high concentration of CCN results in the creation of many small droplets which are unable to coalesce into large rain droplets, thus inhibiting the formation of warm rain. The vertical region where the bulk of this rainfall occurs is referred to by Rosenfeld and Lensky as the rainout zone. The effective particle size remains constant throughout this region as there is a balance between droplet growth from coalescence and loss of droplets through precipitation.

The mixed-phase region begins after rainout region and once the cloud temperature has dropped below $0^\circ C$. It is so named as in this region supercooled liquid droplets and ice crystals may coexist. Below $0^\circ C$, liquid droplets may freeze into ice crystals however this change is not instantaneous, leading to a vertical transport of super-cooled water in a convective cloud. Water droplets will not freeze instantaneously until they fall below the homogeneous freezing temperature. The exact value of the homogeneous freezing temperature may vary due to local conditions however it is typically taken to be in range from $-37^\circ C$ to $-40^\circ C$. In order to form ice crystals above this point, ice forming nuclei (IFN) must be present in order to trigger heterogeneous freezing. Many aerosols are able to act as an IFN and CCN however certain aerosols may only be effective at triggering either droplet or ice formation. Once formed, ice crystals can grow rapidly resulting in an increase in the particle effective radius r_e of the cloud. This also results in a large release of latent heat which allows sustained updrafts to support the increased weight of the larger particles[15]. There is currently no clear consensus

on the role of updrafts inside the mixed-phase region which are typically large inside the eyewall and other convective clouds. Korolev has suggested that the typically important Wegener-Bergeron-Findeisen (WBF) process, which allows rapid ice growth at the expense of supercooled droplets is inhibited in strong updraft clouds [16]. Instead it is suggested that for the case of strong updrafts, there is simultaneous growth of supercooled droplets and ice.

Once there is little or no liquid droplets left in a cloud it is said to be fully glaciated. This is achieved when the temperature in the cloud reaches the *glaciation temperature* T_g . Above this point, the effective radius of the cloud remain either constant or starts to decrease due to the “size sorting” effect[15]. This occurs because the largest ice particles eventually cannot be transported any higher by the updrafts and either remain at a constant level or precipitate out of the cloud. The glaciation temperature is still a poorly understood quantity and it has not been thoroughly investigated in the context of TCs before. Previous studies by Rosenfeld have linked variations in the glaciation temperature of maritime and continental convective clouds to the presence of large aerosols including desert dust, air pollution and smoke from forest fires[17]. The glaciation temperature is also known to be linked to the updraft speed inside the cloud with higher updrafts resulting in cooler T_g and the strongest updrafts all resulting in glaciation at the homogeneous freezing temperature. Models have suggested that desert dust in particular could have a significant effect on the development of Atlantic hurricanes[18], however such models also typically do not factor in a complete microphysical description.

1.3 The effect of sea spray aerosol on TCs

The high winds in a TC can also have a profound effect on the ocean surface. In particular, Emanuel has shown that the maximum wind speed of a TC depends greatly on the coefficient of drag C_D between the air and ocean[19]. For low wind speeds (up to $\approx 20\text{ms}^{-1}$) over the open ocean it has been measured that C_D increases with wind speed[20]. It has been predicted by Emanuel and shown by Donelan however that above 33ms^{-1} C_D reaches a maximum value of around 2.5 and at very high speed ($> 50\text{ms}^{-1}$) it begins to decrease. Powell et al hypothesized that this may be the result of small patches of sea foam being formed from the agitation of the sea surface[21]. In wind speeds of greater than 50ms^{-1} Powell suggested that the entire sea surface may be covered by a layer of foam up to 50cm thick. The high vertical wind speed near the eyewall can then allow this foam layer to be lofted into the cloud creating large quantities of sea salt aerosol (SSA). This aerosol is usually comprised of sea salt crystals as well a large amount of organic matter and is classed as being a giant or ultragiant aerosol. SSA is also a highly effective CCN, promoting the rapid formation of droplets in clouds and releasing latent heat. An idealized model developed by Shpund has suggested that the presence of SSA in the eyewall can result in an increased intensity of the TC[22] and a model developed by Jiang et al has shown an increase in the updrafts in the eyewall with an increased concentration of SSA[23].

1.4 Remote Sensing

Observations in atmospheric physics including for TCs can be collected from a variety of sources which can be divided into two categories: in-situ and remote sensing. In-situ measurements refer to data collected from instruments making direct contact with the weather

phenomena in question including data from ground stations, buoys and aircraft. Remote sensing, refers to measurements collected by instruments remotely to the site of interest, typically from satellites or aircraft. Recently, the resolution of remote imagers has improved drastically with satellite radar now able to resolve features at a resolution down to 5m.

Remote sensing has many advantages for observations of TCs. The environment in the eyewall is an extremely violent environment and remote sensing prevents the need to design an instrument to withstand this. Additionally, an instrument on-board a polar orbiting satellite is able to collect observations across the entire planet multiple times a day for multiple years. This provides a consistent set of observations for all TCs. The concept of “levels” is used commonly with remote sensing data to refer to the degree of processing that has been applied to an image. The raw data as captured by the sensor is referred to as Level 0. This investigation utilized Level 1B data, which refers to raw data which has been processed into sensor units. Table 1 shows the remote sensing bands used in this investigation alongside their associated sensor units that the data was made available in.

1.5 Objectives

The main objectives of this investigation were to determine whether any variation in glaciation temperature T_g or particle size is seen between the eyewall and TC periphery. If a variation is found, it would agree with previous predictions for the presence of SSA in the eyewall which has also been associated with increased cyclone intensification[22] in idealized models. To accomplish this, we utilized images from the VIIRS instrument onboard the Suomi NPP satellite to obtain a catalogue of eyewall and external periphery images in a range of TCs from 2012. The high resolution of the imaging VIIRS band is able to directly image a profile of temperature against reflectance in $3.7\mu m$ channel for the entire eyewall which has not been attempted previously. From these profiles we first aimed to test if there were any variations in T_g between the eyewall and external region and whether these were related to TC intensity or the basin of formation.

Additionally we aimed to establish whether there were any differences in the droplet size between the eyewall and TC periphery. Recent radar observations of 2 TCs in the North Indian Ocean have shown that the effective radius in the eyewall is $\approx 10\mu m$ smaller than those from the periphery[24]. This seems to be consistent with the increased production of SSA near the eyewall which should lead to smaller droplets. We aim to see if this is seen across the catalogue of intense TCs and if so, whether the difference can be explained in the production of SSA at the eyewall.

2 Method

Images from the VIIRS (Visible Infrared Imaging Radiometer Suite) instrument onboard the Suomi NPP satellite were used in this investigation to measure temperature–reflectance ($T - \rho$) profiles in the eyewall and periphery of intense TCs. The main advantage of using images from VIIRS is their high spatial resolution of up to 375m at nadir in its five imaging bands[25]. This is vast improvement over alternative instruments such as MODIS (Moderate Resolution Imaging Spectroradiometer) which has a peak resolution of 1km at nadir. VIIRS

Band	Central wavelength(μm)	Bandwidth(μm)	Resolution (m)	Sensor Unit
I1	0.64	0.08	375	Reflectance (%)
I4	3.74	0.38	375	Brightness Temperature (K)
I5	11.45	1.90	375	Brightness Temperature (K)
M15	10.76	1.00	750	Brightness Temperature (K)
M16	12.012	0.95	750	Brightness Temperature (K)

Table 1: Properties of the VIIRS bands used in this investigation. Data obtained from NOAA [26].

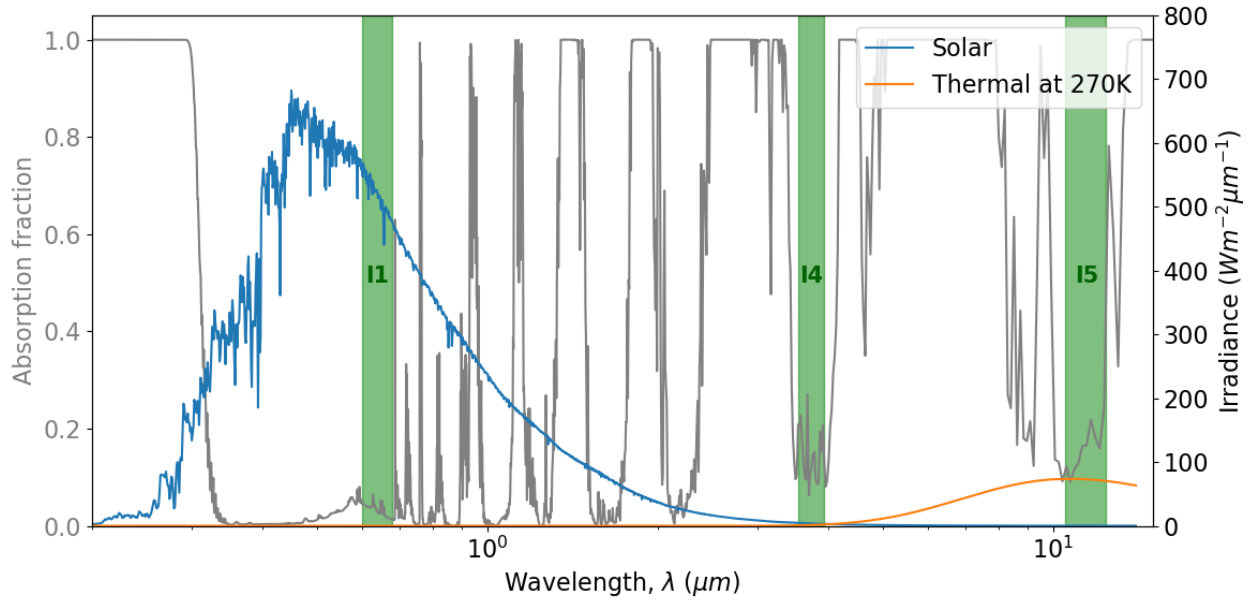


Figure 1: The VIIRS imaging bands used in this investigation shown with respect to the atmospheric absorption spectrum and the solar and thermal irradiances. The absorption spectrum is determined at the top of atmosphere looking towards the Earth’s surface. The moderate resolution M15 and M16 bands, not shown on this figure, overlap with the I5 band.

also has several moderate imaging bands which have a resolution of 750m, which are usually used in retrieval of cloud properties. The swath width of VIIRS of 3060km is also an improvement over MODIS. The images used in this investigation are in the public domain sourced from the NASA LAADS (Level-1 and Atmosphere Archive and Distribution System) archive. Images provided from LAADS are provided in 6-minute intervals corresponding to 6464 lines or an approximate distance of 2400km. The Suomi NPP satellite is positioned in a solar-synchronous polar orbit which gives it near global coverage with separate day and night images. Only the day images were used in this investigation as we were interested in measuring the reflectance of clouds which required the clouds to be illuminated.

2.1 Determination of cloud temperature and $3.7\mu\text{m}$ reflectance

The Earth’s atmosphere is opaque to most wavelengths of up-going radiation from the Earth’s surface with the exception of the “atmospheric windows” where it is mostly transparent. The location of these windows is determined by Rayleigh scattering, which inhibits transmis-

sion in sub visible wavelengths, and atmospheric molecules which absorb strongly at certain wavelengths in the infrared. This can be seen in figure 1 where the atmospheric absorption fraction can be seen as a function of wavelength. The VIIRS imaging bands in Table 1 are also shown and it is seen that these overlap with locations of low atmospheric absorption. Also shown in figure 1 are the irradiances from the sun and a blackbody at a temperature of 270K. Clouds both inside the eyewall and external can be assumed to be optically thick, this enables them to be efficient blackbody emitters.

As seen in figure 1, the I5 band of VIIRS overlaps with the peak of blackbody spectrum at a temperature of 270K. As this also corresponds to a region of low absorption, brightness temperatures of a cloud measured in this region will be very close to the true temperature of the cloud. For the VIIRS instrument, Rosenfeld has shown that the temperature accuracy from the I5 band is $\pm 0.8\text{K}$ at a temperature of 210K[27]. Inside a cloud, the temperature can be related to the altitude by the moist adiabatic lapse rate Γ_m which is approximately 7 K/km . This is a near linear relationship thus a profile of decreasing temperature can be considered equivalent to a profile of increasing altitude.

Nakajima and King showed that, assuming a cloud is optically thick, the cloud effective radius r_e [13] is proportional to the negative logarithm of the $3.7\mu\text{m}$ reflectance. This is because water absorbs strongly in the $3.7\mu\text{m}$ channel, and thus droplets with a larger r_e will reflect less light at this wavelength resulting in a lower reflectance. To determine an exact relation between $\rho_{3.7\mu\text{m}}$ and r_e requires knowledge of the optical geometry of the system, which can be non trivial for the eyewall. At the high resolutions used in this investigation, three dimensional effects such as shadowing and internal reflections became non-negligible and the plane-parallel assumption needed to calculate r_e does not hold. As such a lookup table for r_e was not used in this investigation unlike previous studies of non cyclonic deep convective clouds done by Rosenfeld [11, 17], Yue[28] and Yuan[15].

As seen in figure 1, the I4 band can be used to obtain the brightness temperature in the $3.7\mu\text{m}$ region. In the case of a cold cloud, the reflectance would simply be the ratio of the radiance measured from the I4 band to the incident solar radiance at $3.7\mu\text{m}$. The brightness temperatures recorded by the satellite can be converted into a radiance spectrum using the Planck equation. As seen in figure 1, at wavelengths close to $3.7\mu\text{m}$ there is both a thermal and solar component of the radiation present. In order to isolate the solar component, the temperature from the I5 band was used to estimate the component of thermal radiation present in the I4 band which can then be subtracted. This leads to the following equation used to obtain the I4 reflectance:

$$\rho_{I4} = \frac{L_{I4} - \int_0^\infty d\lambda B_\lambda(T_{I5})\Phi_{I4}(\lambda)}{\cos\theta F_0/\pi - \int_0^\infty d\lambda B_\lambda(T_{I5})\Phi_{I4}(\lambda)} \quad (2)$$

In the above, F_0 is the incident solar flux in the I4 band, θ is the solar zenith angle and Φ_{I4} is the spectral response of the satellite in the I4 band. The response term accounts for the fact that VIIRS is not uniformly sensitive to all wavelengths inside a given band. Data for the spectral response of the VIIRS bands was obtained from the Global Space-based Inter-calibration system and the calculations were done using the pySpectral library, a component of the pyTroll project[29].

2.2 Masking of non-cloud pixels in VIIRS images

The location and intensity of TCs was obtained from the IBTrACS (International Best Track Archive for Climate Stewardship) dataset[30]. This contains combined surface, ship and satellite observations from multiple meteorological agencies across the world to obtain position and intensity estimates for every TC on a 3 hour interval. This dataset extends back to 1980 however images from VIIRS are only available going back to 2012 which limited the number of TCs which we were able to investigate. For each 3 hour interval containing a TC of category 4 or 5, the LAADS database was queried to obtain the appropriate VIIRS swath images, if any exist.

Once swath images were obtained they were first resampled to a uniform grid in order to remove the so called “bowtie” effect which occurs at the edge of VIIRS swath images. This grid was then centered on the eyewall of the TC. The next stage was the identification of the pixels making up the TC eyewall and deep convective clouds in the TC periphery; this was achieved by applying multiple masks to the image leaving only relevant pixels. A summary of all the masking steps conducted for both the eyewall and periphery is seen in figure 2.

The first mask that was applied was a simple temperature cut-off. When creating $T - r_e$ profiles to determine T_g we utilized the same upper cut off as Yuan of 260K[15]. As this is considerably below the freezing point of water, this ensures that the profile contains only the mixed-phase and glaciated regions. When generating profiles to investigate droplet growth we utilized a higher cut-off of 280K, which is still far cooler than the SST but sufficiently warm to include the rainout regions which is dominated by liquid droplets. A lower cut-off of 220K was chosen to mask out pixels present in the upper cloud shield of the TC.

The use of a lower limit at 220K also had the effect of filtering out the majority of thin cirrus pixels from the image. Whilst VIIRS provides a dedicated band for the detection of this cloud type studying images of eyewalls in this band showed little to no thin cirrus present in the eye. Outside the eyewall, the overwhelming majority of thin cirrus identified in this band was found to be already masked by the temperature cutoff.

We also utilized the reflectance in the visible I1 band to mask non cloud and shaded pixels. As seen in figure 1, this band overlaps strongly with the solar component of the received radiation which allows I1 to be used to distinguish between shaded and non-shaded pixels. Due to the low albedo of the ocean, the I1 band can also be used to mask ocean pixels. Yue et al [28] has suggested that a visible reflectance mask of all pixels less than 30% is sufficient to eliminate non cloud pixels in maritime environments. We utilized this restriction in addition to a mask of all pixels with a reflectance less than the mean I1 value of each cell plus 1 standard deviation of the I1 reflectance. This was done to ensure that shaded pixels were not included in profiles which was particularly relevant for the eyewall, where the circular geometry allows shadows to form from the opposite side of the eyewall.

The final adjustment made was a filter for multi-layered clouds and water vapour which was achieved using a method described by Rosenfeld[27]. This required the calculation of the brightness temperature difference (BTD) between the $12\mu m$ and $11\mu m$ bands as seen in table 1. For VIIRS these channels only exist for the moderate resolution and both overlap with

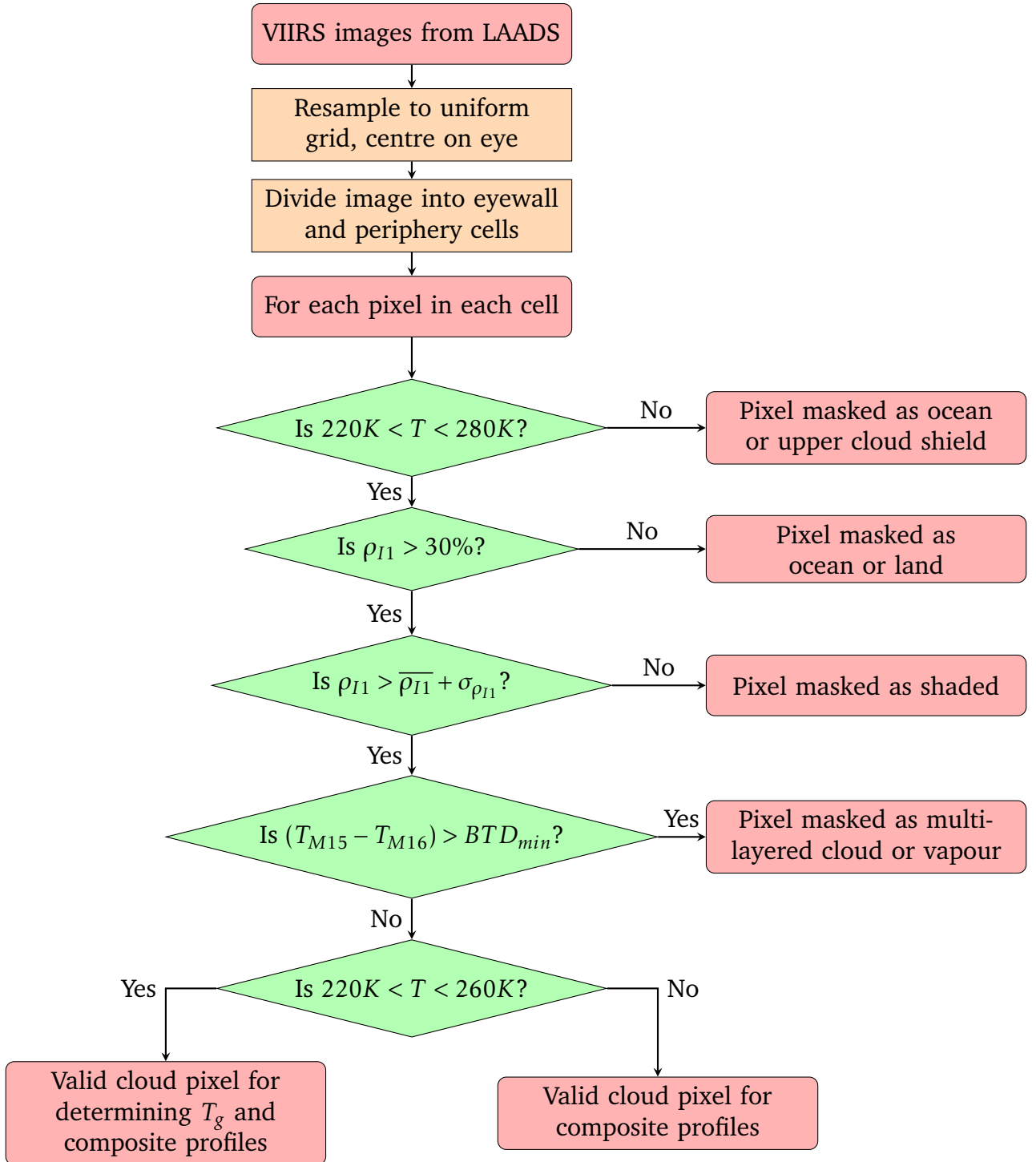


Figure 2: Demonstration of the various masking conditions applied to each condition for determining T_g as well as the composite profiles.

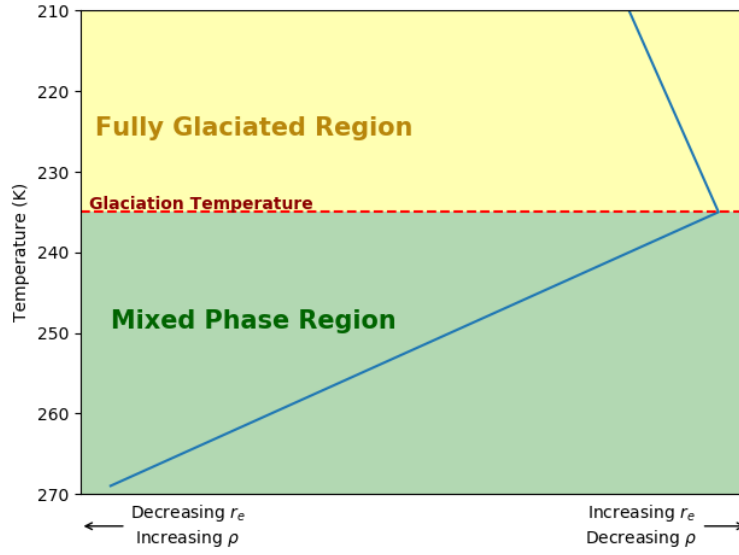


Figure 3: Demonstration of the simple linear piecewise model to relate how the $3.7\mu\text{m}$ reflectance and thus the cloud effective radius evolves with temperature. The glaciation temperature marks the transition between the mixed phase and fully glaciated region. Adaptation of figure from Yuan et al[15].

the imaging I5 band, thus the BTD was calculated in the moderate resolution and then up-scaled to the imaging resolution using nearest neighbouring sampling. For each individual eyewall or cell in the TC periphery considered, pixels were sorted by temperature into 1K wide bins and the 25th percentile BTD for each bin was calculated. Inoue has shown that the BTD must monotonically decrease in the absence of overlying multilayer clouds and water vapour[31]. This requirement was enforced by iterating from high to low temperature and only allowing the BTD to remain constant or decrease with decreasing temperature. Pixels were then masked if they had an individual BTD greater than the adjusted BTD, BTD_{min} for the corresponding temperature bin.

2.3 Identification of the Glaciation Temperature from $T - \rho$ profiles

As discussed in section 1.2, inside a deep convective cloud there are typically 5 distinct stages of droplet growth of which the mixed-phase and fully glaciated regions were the focus of this investigation. The glaciation temperature T_g occurs at the boundary between the mixed phase region and the fully glaciated region and appears as a turning point in the effective particle radius r_e [15]. As described above, r_e is proportional to the negative logarithm of the $3.7\mu\text{m}$ reflectance for clouds of high optical depth such as those associated with TCs.

In order to determine the glaciation temperature from the profiles of temperature and $3.7\mu\text{m}$ reflectance a simple model of the particle growth was used. To a first approximation, particle size was taken to increase linearly inside the mixed-phase and decrease linearly or remain constant once the clouds were fully glaciated. In our model, the glaciation temperature is located at the piecewise join between these two regions and appears as a discontinuity in the derivative of the profile. This model is demonstrated in figure 3. In order to fit this model to a profile, the individual pixels were binned by temperature and the mean reflectance

ρ for each bin was calculated. By taking the mean of each bin the impact of random error present due to the viewing geometry, optical depth and scattering for each pixel should be reduced. As the random error for an individual pixel in the image can be considerable a large number of pixels are needed to generate an accurate profile. As such we required at least 100 unmasked pixels to present in the image prior to the temperature binning. The model was then fitted to the binned $T - \rho$ profile using a least squares optimizer from the SciPy package in Python, where T_g was a fitted parameter. This allowed its value and error was determined directly by the fitting algorithm.

Only profiles which had physical feasible glaciation temperatures were used in the catalogue of TCs. A physically feasible T_g was defined as being in the range: $-10^\circ\text{C} > T_g > -45^\circ\text{C}$. This range covers from the lower limit of the homogeneous freezing temperature up to the temperature where the mixed-phase region typically begins. A 5°C margin was included on the lower limit as the random error for a given fit is symmetric and so it is possible to observe a valid profile with a fitted $T_g < -40^\circ\text{C}$. If these cooler T_g fits were negated it would introduce a systematic bias into the results towards warmer temperatures. The goodness of fit was determined by calculating the Normalized Root Mean Square Error (NRMSE) defined as:

$$\text{NRMSE} = \frac{1}{\rho_{\max} - \rho_{\min}} \sqrt{\frac{\sum_i (\rho_i - f_i)^2}{N}}, \quad (3)$$

where ρ_i and f_i are the measured points in the profile and fitted profile points respectively. The NRMSE represents the average distance from the regression line to the profile data points such that a lower value represents a better fit. This value was normalized to the range of reflectance seen in the profile, $\rho_{\max} - \rho_{\min}$ to make it possible to compare goodness of fit between profiles with differing reflectance scales. For a fitted profile to be added to the catalogue it was required to have a $\text{NRMSE} \leq 0.3$.

2.4 $T - \rho$ profiles in the eyewall

The high resolution of VIIRS images makes it possible to directly observe and measure the $T - \rho$ profile in the eyewall and this is demonstrated in figure 4. For each TC image masked as described in section 3.2, eyewall pixels were defined as being located in a square cell centered on the iBTrACS TC position. The size of the cell was set at twice the radius of maximum wind of the TC as determined from the best track data. The glaciation temperature was determined by the fitting the model described in section 3.3 directly to the $T - \rho$ profile. Eyewall images with non-physical glaciation temperatures or profile fits were rejected from the catalogue. Figure 5 shows the result of the masking applied to an image of TC Hector and figure 6 shows the resultant profile with the piecewise model fit applied. Both axes are inverted on this profile as a decrease in temperature corresponds to an increase in altitude and a decrease in I4 reflectance corresponds to an increase in effective radius. This example profile has a glaciation temperature of $T_g = 235.6 \pm 1.7\text{K}$ and the profile has a NRMSE of 0.09, below the maximum permitted value of 0.3. As such this profile was added to the catalogue.

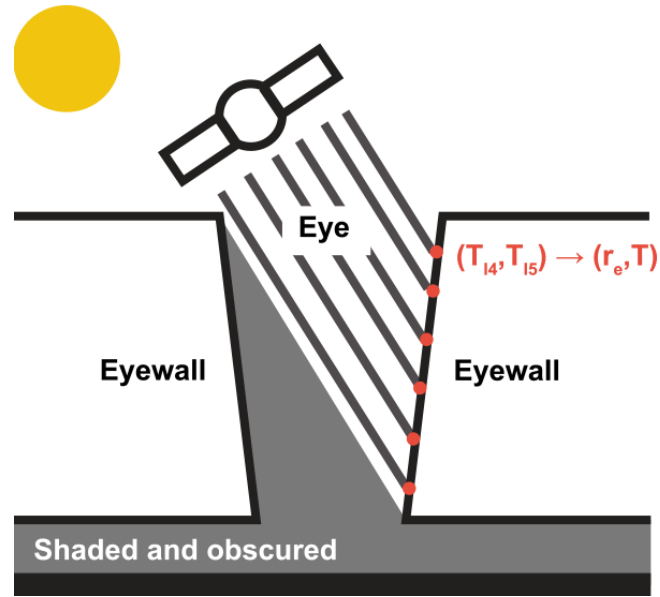


Figure 4: Demonstration of how the $T - \rho$ profile can be measured in the eyewall via remote sensing. The large scale of the eyewall means that there will be many individual data points present in the eyewall allowing a clear profile to be obtained.

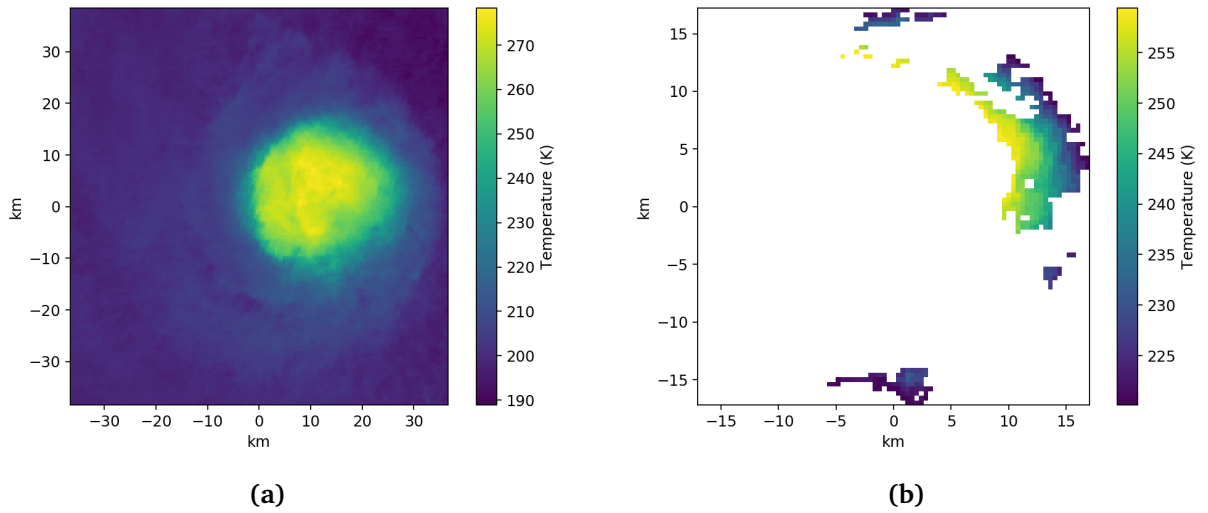


Figure 5: Demonstration of the masking process applied to the eyewall thermal image of TC Hector with a) displaying the original image and b) the result after the masking is applied.

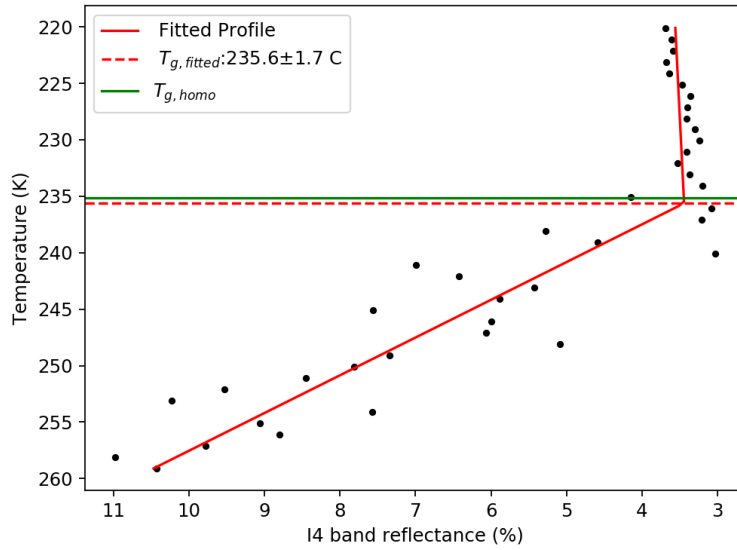


Figure 6: The piecewise model described in section 2.2 fitted to the profile from the masked eyewall image seen in figure 5b. The fitted T_g is calculated to have a value of $235.6 \pm 1.7K$, close to the homogeneous freezing temperature, and the NRMSE has a value of 0.09 so this profile was added to the catalogue.

2.5 Determination of $T - \rho$ profiles in the TC periphery

Directly obtaining the $T - \rho$ profile as demonstrated in figure 4 was not possible in the TC periphery as clouds here do not possess an as defined vertical edge compared to the eyewall. Thus using the eyewall method in the periphery would require developing a method to detect individual cloud edges and whilst methods exist to be able to do this they typically rely on lower resolution image data, which would negate the benefit of the high resolution of the VIIRS imaging bands. Rosenfeld and Lensky have demonstrated that it is possible to obtain $T - \rho$ profiles by utilizing cloud top measurements from a large number of independent convective clouds in a region[32]. This is known as time-space exchangeability and relies on the assumption that all clouds in a local region in both space and time will have similar properties. Thus by measuring a sufficiently large sample of various cloud tops which will all be located at different altitudes it is possible to estimate the vertical profile for a cloud group in the TC periphery. In this investigation we utilized large cells of 192×192 pixels which corresponded to a distance of 72×72 km. This size was chosen as a balance between the need to include as many pixels as possible whilst keeping the cell small enough that time-space exchangeability holds. For each intense TC identified from the iBTrACS dataset, the cells were tiled onto a large $16^\circ \times 16^\circ$ grid centered on the eye of the TC. Cells that overlapped the eyewall of the TC were ignored as the profile here was measured directly as shown in section 2.3. In addition, the I1 mask described in section 2.2, resulted in the cloud shield and underlying rainbands. As was done with the eyewall, a cell was ignored if it had a non-physical glaciation temperature or the if the NRMSE for the piecewise model in figure 3 was below 0.3. Cells containing fewer than 100 individual pixels were ignored as they do not contain enough pixels to create a temperature profile. A demonstration of this method on TC Hector can be seen in figure 7 with the resultant profile from the cell seen in figure 8.

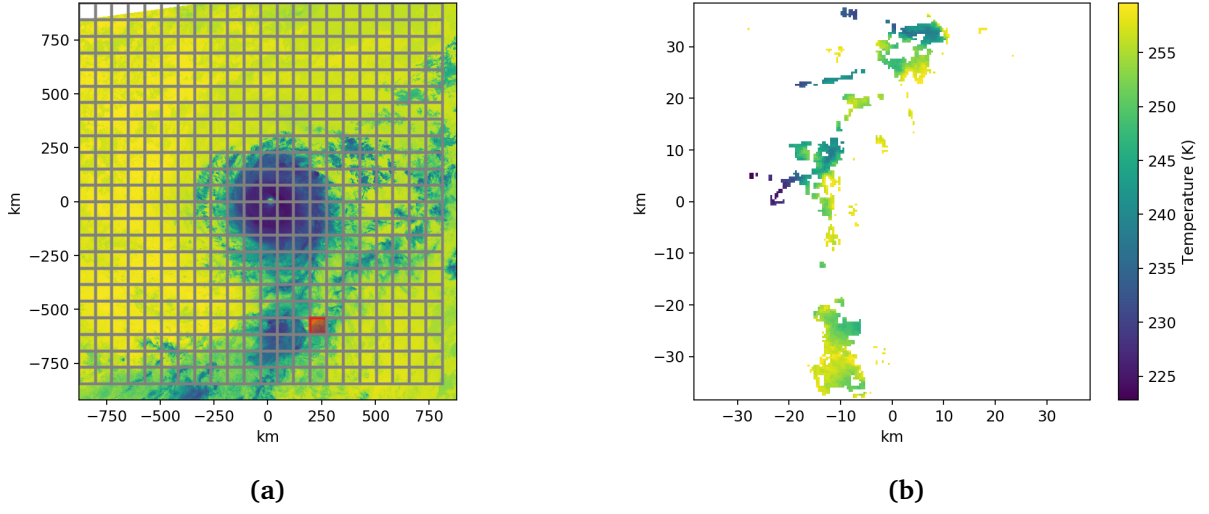


Figure 7: Demonstration of how T_g is determined for a cell in the cyclone periphery. In a), the grid of all potential periphery cells is displayed with the example cell displayed in b) highlighted in red.

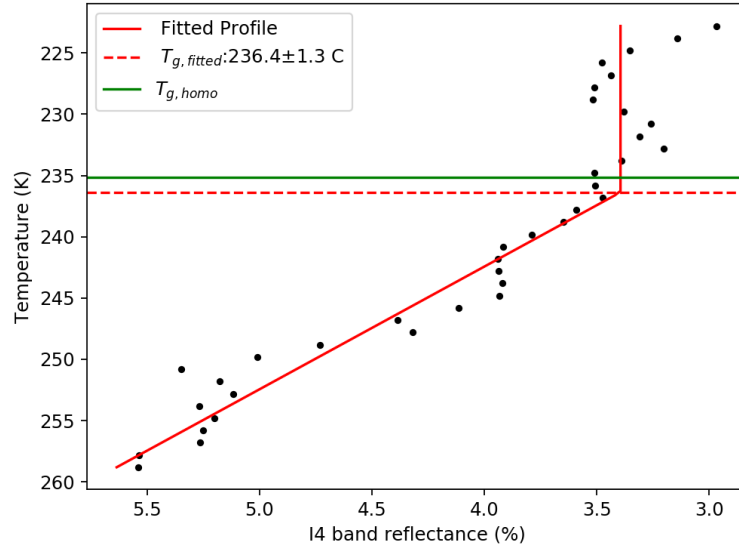


Figure 8: Sample profile from the cell displayed in figure 7. The T_g has a fitted value of 236.4 ± 1.3 K and the NRMSE has a value of 0.067 so this profile was added to catalogue of periphery profiles.

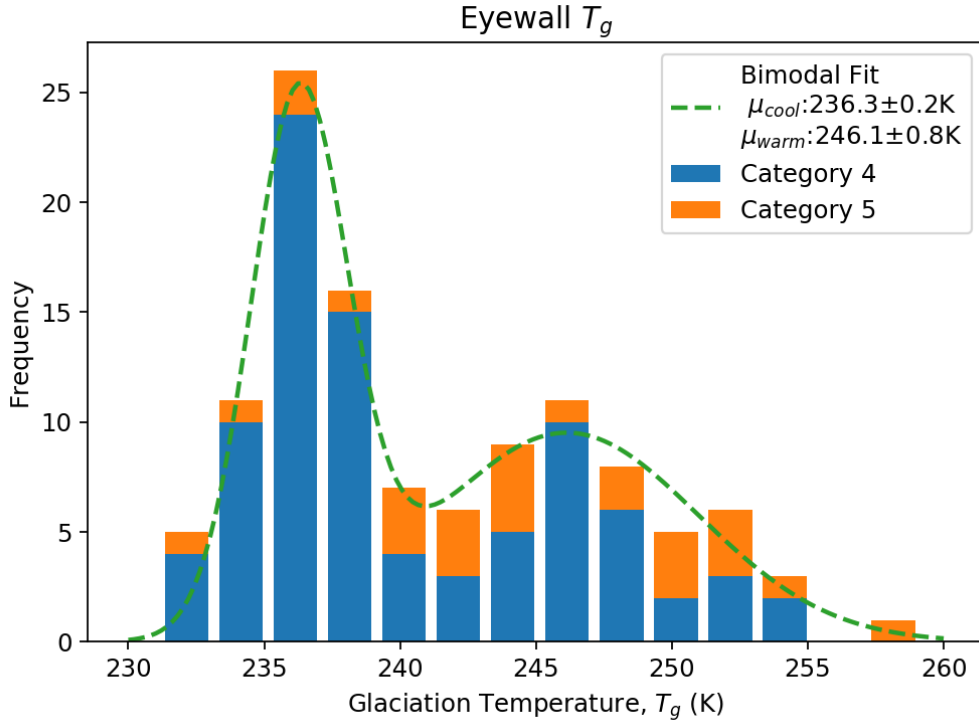


Figure 9: Distribution of glaciatiion temperatures, T_g inside the eyewall filtered by TC intensity. A bimodal fit has been applied, with two peaks: a cool peak at μ_{cool} and warm peak at μ_{warm} .

3 Results

Applying the method described above for all intense TCs imaged by VIIRS since 2012 yielded a catalogue of 118 TC images with acceptable eyewall profiles. The images in the catalogue were captured from 75 distinct TCs, thus for some TCs the $T - \rho$ profiles were measured at multiple intervals during the TCs lifespan. From the iBTraCS dataset, from 2012 until the present there were a total of 163 named storms that reached category 4 for at least 3 hours, thus our method was only able to catalogue just under half of all available storms.

In the catalogue a total of 69 images of category 4 TCs are present compared to 21 images of category 5 TCs. The majority of TCs captured were from the West (60) and East (20) Pacific basins, which was to be expected as these basins were by far the most active during this time however there seems to be a lower than expected number of just 12 in the North Atlantic. This was to be expected however as a result of a period of record low activity that was present in this basin from 2005 until 2017 where no TCs above category 3 intensity were observed.

3.1 Distribution of glaciatiion temperatures in the eyewall and periphery

The distribution of the glaciatiion temperature T_g inside the eyewall was determined placing all T_g values in the eyewall into 2K wide bins which is seen in figure 9. The resultant distribution unexpectedly contained two peaks, implying the presence of two classes of TC eyewalls:

a “warm” class and a “cool” class. A bimodal distribution was fitted to this distribution as seen in figure 9 and the location of the peaks calculated. The cooler peak was calculated to be centered on a temperature of $\mu_{cool} = 236.3 \pm 0.2K$, whilst the warmer peak has a temperature of $\mu_{warm} = 246.1 \pm 0.8K$. The low error in both peaks means that these peaks were statistically significant from each other at greater than 2σ of error. Taking the minimum in the fitted binomial distribution as the separator between the warm and cool classes, which has a value of $T_{min} = 240.9K$, then two groups are divided evenly with 66 TC profiles in both the “cool” group and 52 profiles in the “warm” group.

The cooler peak lies very close to the homogeneous freezing temperature indicating that in eyewalls located in the leftmost peak, supercooled liquid is transported near to the point of homogeneous freezing with heterogeneous processes having little effect. This behaviour would agree with a model developed by Korolev relating updrafts to ice formation[33]. This model suggests that for clouds which contains an updrafts above $4ms^{-1}$, that homogenous freezing is the dominant mechanism of ice formation with the effect of the WBF process becoming negligible. As the typical updraft velocity in the eyewall can be in excess of $10ms^{-1}$ however it would be expected that the majority of eyewall profiles should have a T_g close to the homogeneous freezing temperature but figure 9 shows that only half the eyewall profiles fit this description with those in the “warm” peak showing a significance departure from the homogeneous freezing temperature of over 10K.

Thus the presence of a warmer class of TCs provide evidence that homogeneous freezing does not take place in all eyewalls. The presence of a warmer class of TC persisted even when considering eyewall images located on each individual side of the swath, indicating that this effect is not a result of the optical geometry. The above distribution for T_g in the eyewall was then compared to the distribution seen in the cells located in the TC periphery, external to the eyewall. Here a departure from bimodality was observed as seen in figure 10. This distribution appears to follow the shape of a skewed normal distribution with a single peak at $236 \pm 1K$, overlapping with the “cool” peak seen in figure 9 and close to the homogeneous freezing temperature. This distribution appeared to be homogeneous across the TC, with the distribution remaining unchanged moving radially outwards from the center for a given TC. In addition for a given TC, there is no difference in the distribution of T_g when considering cells located in advance of and behind of a given TC track. Furthermore, figure 10 shows that the distribution in the periphery appears identical for both category 4 & 5 TCs.

The TC periphery distribution in figure 10 is in clear contrast to that seen in figure 9 however one factor that must be considered is that the external distribution contains a factor of 100 T_g points than for the eyewall. A Kolmogorov–Smirnov (KS) test was performed to calculate the significance level at which the null hypothesis that the eyewall and periphery distributions are identical can be rejected. This test yielded a KS statistic of 0.157 with a corresponding p value of 0.006. Thus it is reasonable that we can reject the null hypothesis at a significance level of 1% and thus the distributions are not identical even when considering the difference in sample size. Thus the bimodality seen in the eyewall is unique to the eyewall and is statistically significant difference to the distribution in the periphery.

The variation in T_g for the eyewall and TC periphery sorted by the basin in which the TC formed was also studied. For the TC periphery in figure 11b, there appears to be no variation

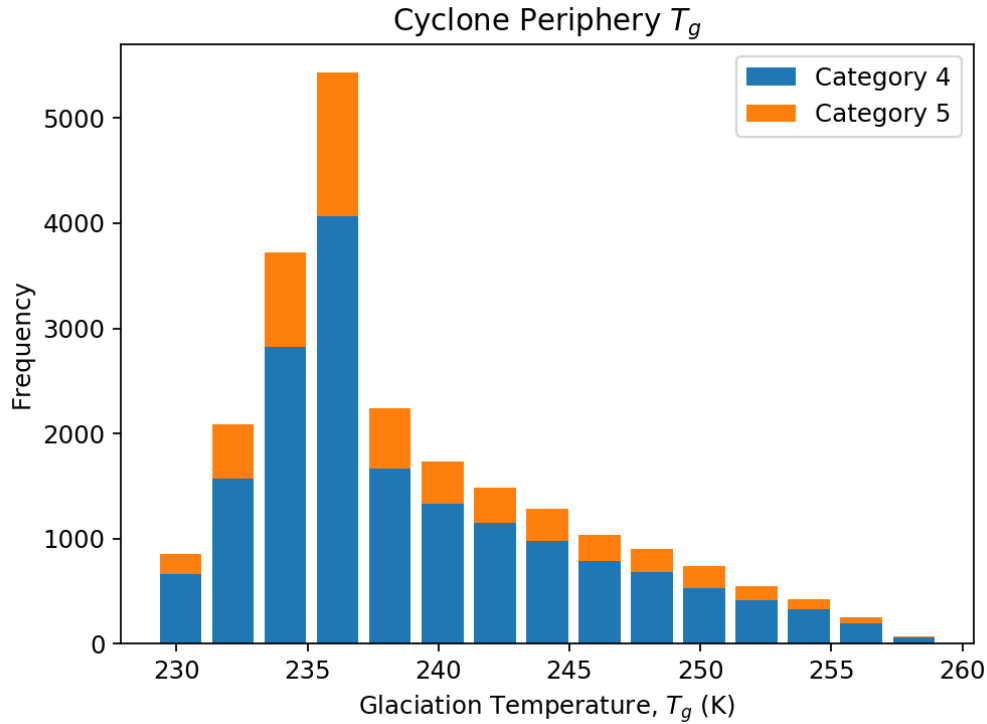
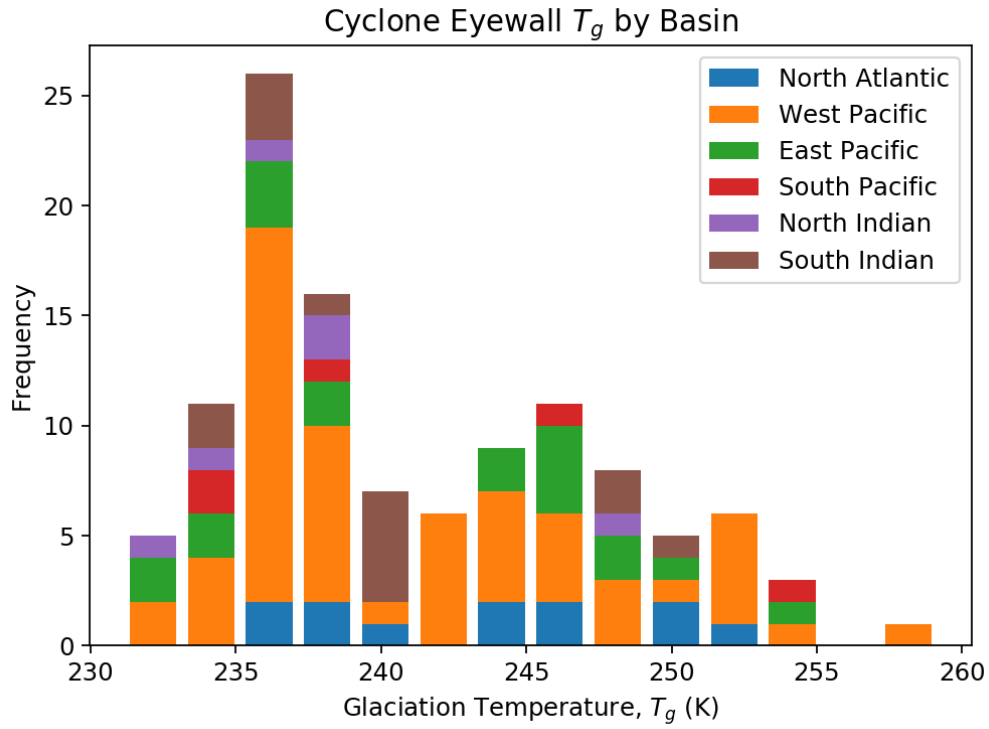


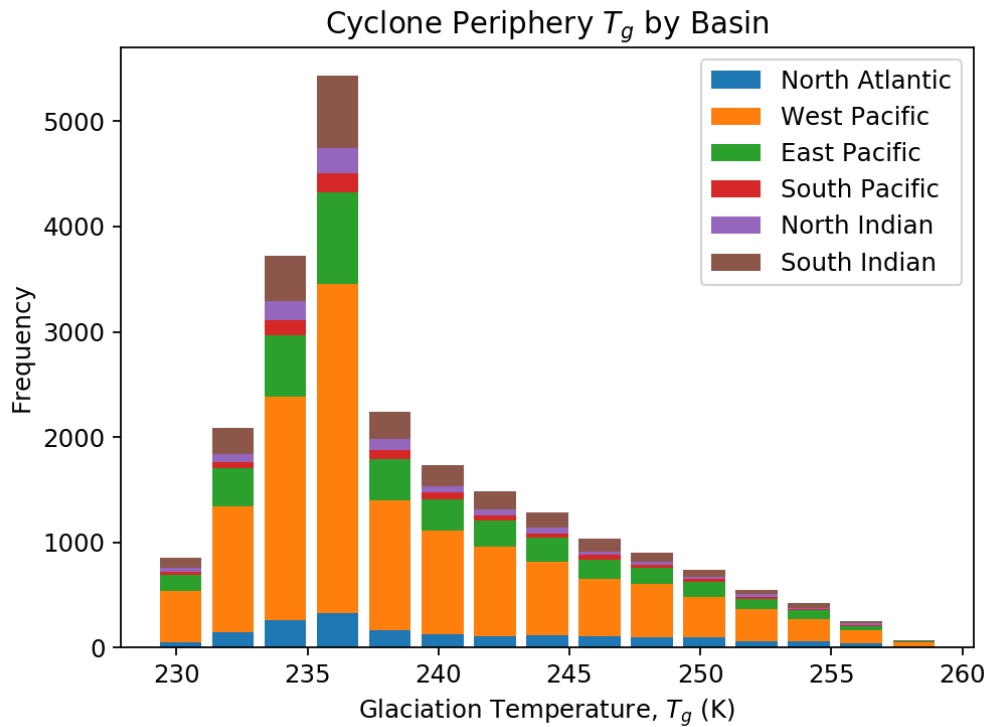
Figure 10: Distribution of glaciation temperatures of cells located in the TC periphery for all catalogued images. This distribution is uni-modal, with a mean temperature of $238.8 \pm 0.1 K$. The same distribution shape can be seen for both category 4 & 5 TCs.

by basin as expected which further demonstrates the robustness of the observation that ice formation in the periphery is dominated by homogeneous freezing. Inside the eyewall, the aforementioned bimodality is most clearly seen in the West Pacific basin which dominates the images in the catalogue. For the other basins there does not appear to be any clear departure for the bimodality with all basins containing at least one cyclone in both the warm and cool peaks however the small sample size means that no firm conclusion can be reached about variations in T_g for basins outside the West Pacific.

Having ruled out any observational effects that could result in a bimodality being present exclusively to the eyewall, we speculated that this effect could be due to the presence of aerosol. As described in section 1.2, aerosol nuclei allow for heterogeneous glaciation which may occur at any temperature below the freezing point of water. Rosenfeld has demonstrated that for polluted maritime and continental clouds in East Asia that there is a reduction of approximately $10^\circ C$ in the T_g compared to pristine clouds[17]. In particular the high updrafts present in both the periphery and the eyewall result in both regions being in an “aerosol limited regime.” Thus, if heterogeneous freezing is occurring it would be exclusively taking place inside the TCs with warmer T_g , corresponding to the rightmost group of TCs seen in figure 9. As figure 10 shows an absence of this shift this aerosol must be exclusive to the eyewall. This presented a challenge as most aerosol is present in the environment long before and after a TC is present. This implies that any effect seen in the eyewall would also be seen in the TC periphery as the intake of environmental aerosol should be similar.



(a)



(b)

Figure 11: Distribution of T_g in the eyewall sorted by basin in which the TC formed for both the eyewall and periphery respectively.

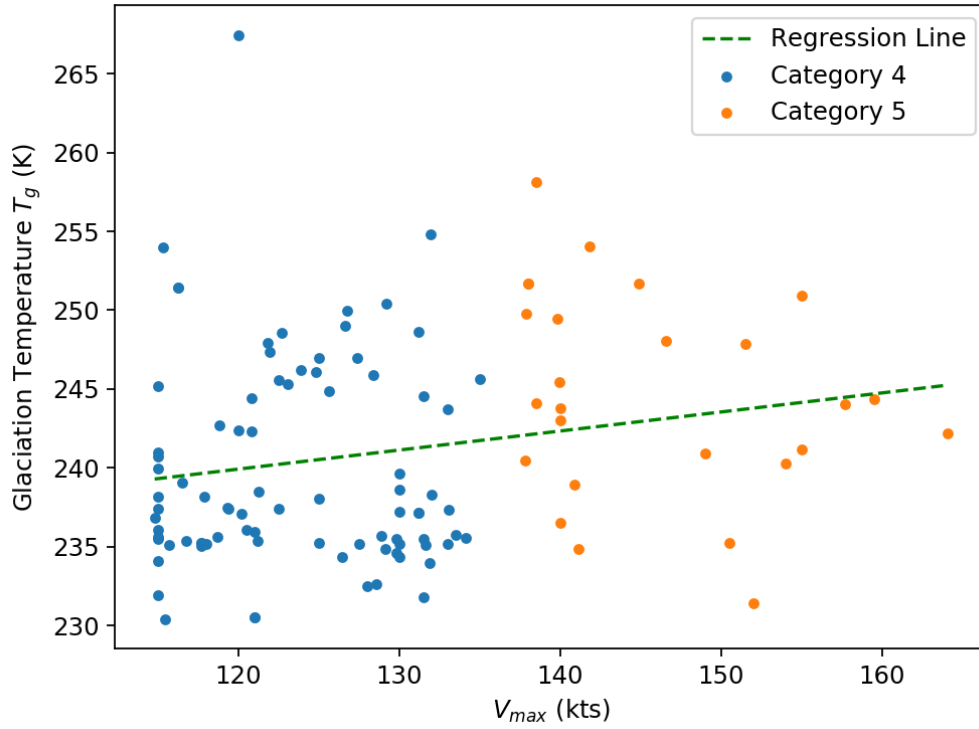


Figure 12: Relationship between the eyewall glaciation temperature T_g and the maximum wind speed V_{max} . A regression line is applied with a gradient of $0.121 \pm 0.055 K/ms^{-1}$ and an R correlation coefficient of 0.20.

There is evidence to suggest that Sea Spray Aerosol (SSA) could be responsible for this bimodality. As described in section 1.1, SSA have been shown to contain large amounts of organic matter as well as sea salt and is an effective CCN and IFN. In particular SSA is considered to be a “giant” aerosol, able to result in a large increase in the precipitation of contaminated clouds[22]. If there is an increase in precipitation owing to SSA in the eyewall then inside the rainout region, then the effective radius r_e must decrease due to the balance between condensation and precipitation in this region. In addition, once supercooled droplets are lofted upwards by enhanced updrafts from the release of latent heat from condensation, the IFN action of SSA allow them to boost heterogeneous freezing. This will then lead to an increase in T_g which is observed in figure 9 in the “warm” peak. The key feature of SSA which makes them a likely candidate for the aerosol present in the eyewall is that their production is directly linked to the wind speed at sea-level. A model developed by Jiang et al for sea salt particles only has determined that the vertical flux of aerosol is $\propto W^{3.41}$ where W is the sea surface wind speed[23]. This model has also predicted that for the case of high sea salt concentrations in the eyewall that precipitation can be increased by up to 120% compared to the low sea salt case, and is further evidence that r_e should be reduced. There is some evidence for a relation between wind speed and T_g can be seen in figure 12 where a weak positive correlation of 0.20 is seen between the maximum wind speed V_{max} and T_g . However the fitted gradient of the regression is $0.121 \pm 0.055 K/ms^{-1}$, with the high error indicating that T_g is only weakly related to wind speed.

One important factor when considering the effect of environmental aerosol is that the catalogue contained an abnormally low number of TCs from the NA basin. As North Atlantic TCs have been speculated to contain large amounts of Saharan desert dust, this would potentially provide an additional warmer shift to T_g that would be seen in the eyewall and periphery however the small sample size present in our catalogue makes it impossible to make a conclusion on this.

The distributions seen in figures 9 & 10 do have some unexplained properties. For one, it is not obvious where there is a bias in periphery distribution towards the homogeneous freezing temperature as opposed to a symmetric normal distribution which is what would be expected for the random error for measurements of a constant value. This could be the result of the hard-cutoff of -45°C used when generating the catalogue of images, however as the distribution has a different shape at temperatures below the peak this does not provide a full explanation. In addition it is not clear why only half of the TCs display a warmer T_g with half of TCs in the catalogue freezing homogeneously. These results could imply that there are issues in using the method described by Yuan et al [15] for estimating the glaciation temperatures in the context of TCs which would need to be investigated further. As such a more robust method of directly comparing the average profiles between the eyewall and periphery was used which to verify if there is indeed SSA exclusive to the eyewall.

3.2 Variation in droplet size between the eyewall and periphery

The apparent difference in glaciation temperature distributions between the eyewall and TC periphery is indicative of aerosol being present exclusively in the eyewall. However studying the T_g distribution alone is not enough to validate any differences in the microphysical behaviour between the two regions. Thus another approach was also used to determine differences between the eyewall and periphery by comparing composite profiles of the eyewall and periphery directly.

To generate these composite profiles for each individual $T - \rho$ profile the 5th, 50th and 95th percentile of ρ was calculated in each temperature bin used to fit the piecewise model as described in section 2.3. At a given T , these values for each image in the catalogue were average together to determine 3 distinct composite profiles in both the eyewall and the TC periphery. The 5th, 50th and 95th percentiles were favoured over the mean in these profiles in order to allow the behaviour of the profiles at extreme values of ρ to be probed.

Figure 13 shows the composite $T - \rho$ profiles between the eyewall and periphery for the 5th, 50th and 95th percentile. In this profile the mixed-phase region can be identified as the region of rapidly decreasing reflectance and hence increasing r_e between 260K and 235K. As this profile is a composite of all profiles and as it has been demonstrated that there is a bi-modal distribution seen in the glaciation temperature, it is not surprising that figure 13 does not show a sharp “kink” as would be expected from our piecewise model discussed in section 2.3. At temperatures above 260K, the reflectances becomes near constant with temperature, this indicates that the cloud is in the rainout region with a balance between droplet formation and precipitation. When evaluating which of these percentiles is more representative of the true particle size inside the eyewall and periphery the brightness temperature difference ratio $\frac{T_{I4} - T_{I5}}{T_{I5}}$ was determined and the result is seen in figure 15. This ratio represents the fraction

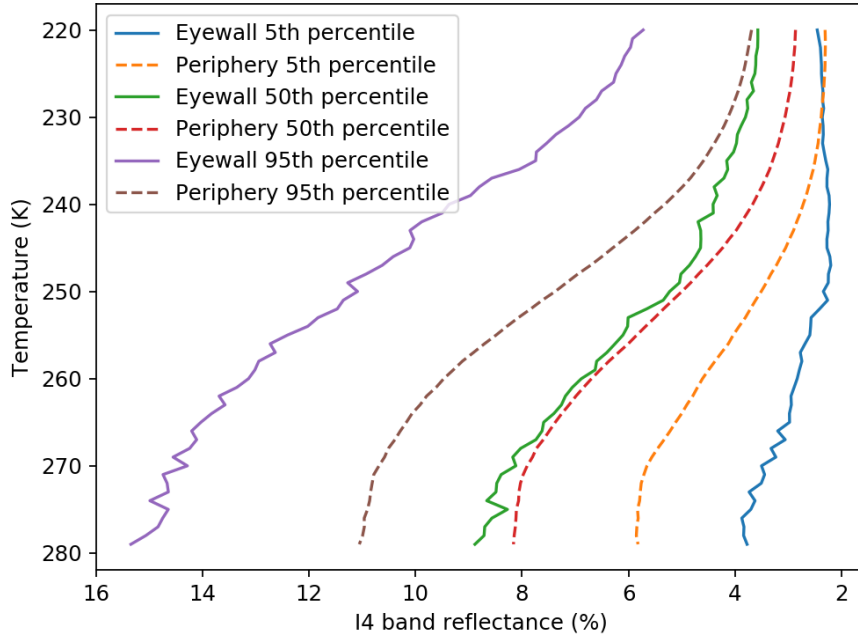


Figure 13: Composite 5th, 50th and 95th percentile $T - \rho$ profiles compared between the eyewall and the TC periphery.

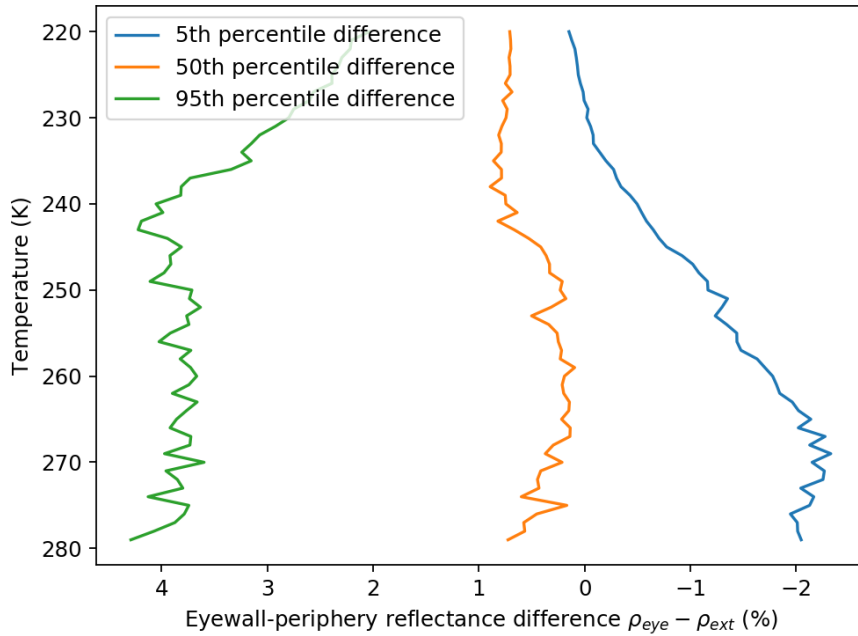


Figure 14: Difference in reflectance ρ between the eyewall and the TC periphery. Positive values of this difference indicate smaller, more reflective droplets, in the eyewall compared to the TC periphery.

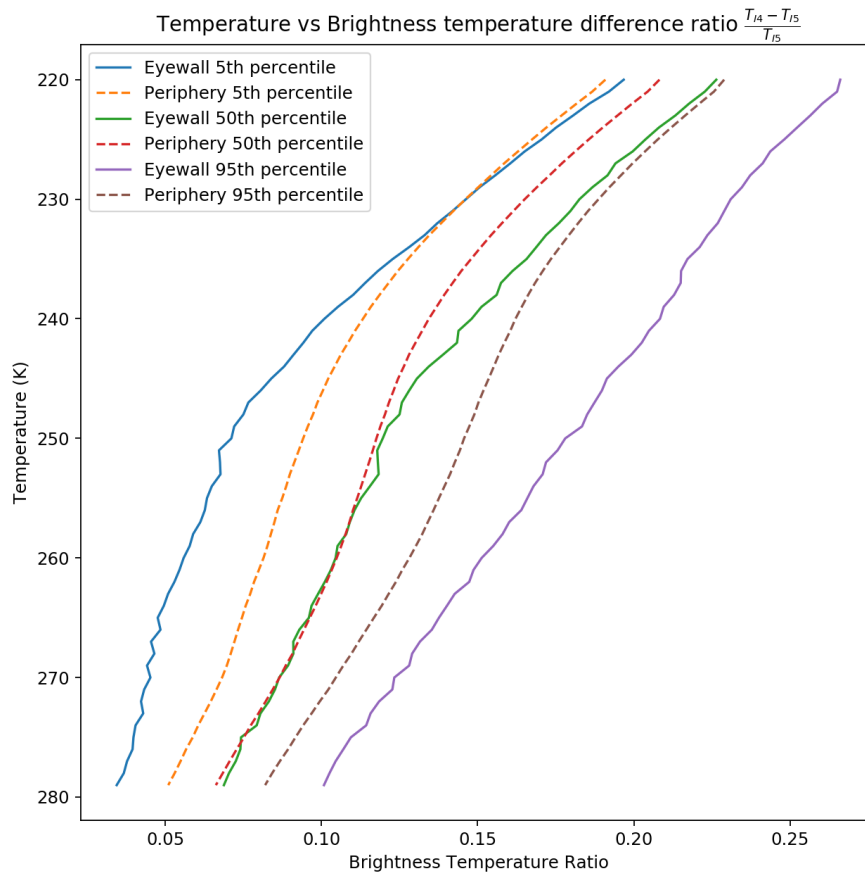


Figure 15: Brightness temperature difference between the $3.7\mu\text{m}$ (I4) and $11\mu\text{m}$ (I5) bands as a ratio to the I5 temperature. The 5th, 50th and 95th percentiles of this ratio are seen for both the eyewall and TC periphery.

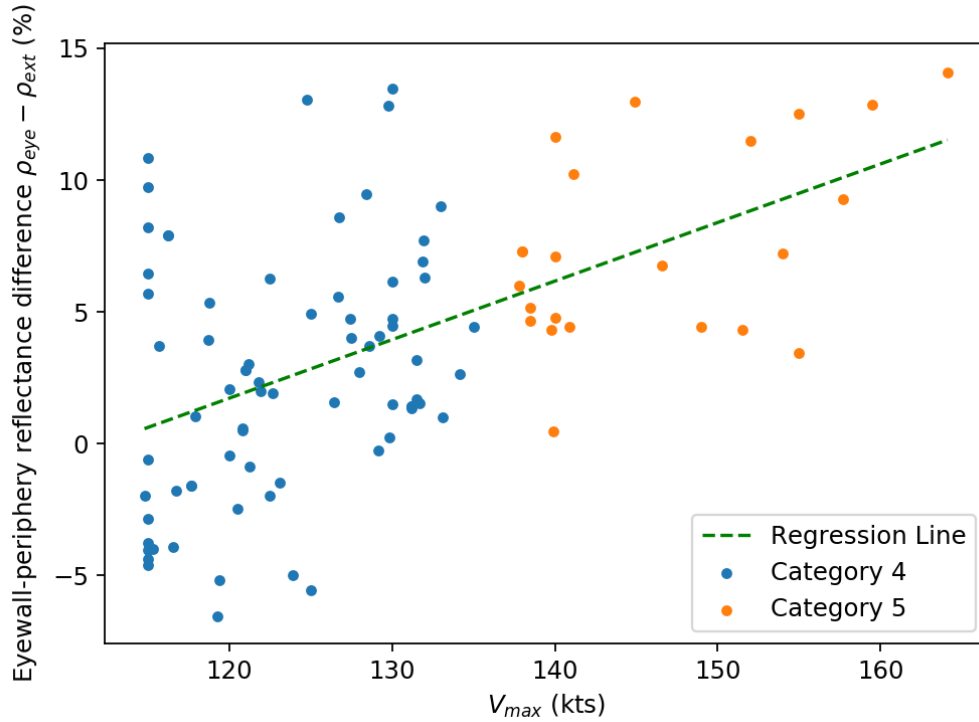


Figure 16: Relationship between difference in reflectance ρ between the eyewall and periphery and the maximum wind speed of the TC V_{max} . The result of a linear regression is seen, with a moderate positive correlation of 0.535 and a gradient of 0.222%/kts

of the brightness temperature in the I4 band that is distinct from the thermal background of the cloud and thus maximising this ratio ensures that the thermal component is minimised. Whilst equation 3 attempts to correct for this component by estimating the thermal component present, choosing the percentile with the highest ratio minimises ensures that the effect of the thermal component is minimized which is especially important when directly comparing the eyewall to the periphery profile. From figure 15, the 95th percentile has the largest value of brightness temperature difference ratio for temperatures in both the eyewall and periphery.

The difference in reflectance between the eyewall and periphery is seen in figure 14, where for the aforementioned 95th percentile the reflectance in the eyewall is greater than that of the periphery at all temperatures. This indicates that the corresponding effective radius inside the eyewall is always less than that seen in the periphery at all altitudes. This is consistent with previous radar measurements made by John et al, where it was estimated that the average particle size inside the eyewall is between $\approx 8\mu m$ less than that seen in the periphery[24]. Shpund found that in $T - r_e$ profiles made using MODIS images for two TCs, that at the cloud top of the eyewall the effective radius was $8 - 12\mu m$ smaller than in the periphery[22]. From this, Shpund constructed a model of an idealized TC where it was found that SSA lead to an increase in ice mass inside the TC and an increase in the TC updrafts. Shpund also found that these effects lead to an increase in the TC intensity in cyclones with high SSA concentrations.

It was also investigated whether there is any variation in the composite profiles seen between category 4 and category 5 TCs. In particular it would be expected that for more intense TCs that the SSA flux into the eyewall would be increased owing to stronger vertical wind speeds as well as increased production of SSA from the bursting of bubbles on the sea surface. Figure 16 shows the difference between the eyewall and periphery reflectances in the rainout region from 260–280K as a function of the maximum horizontal wind speed of the TC, V_{max} , with a linear regression applied with a gradient of $0.222 \pm 0.036\%/kts$. The R correlation of this regression has a value of 0.535, implying a moderate positive correlation between V_{max} and the reflectance difference. This relationship with V_{max} is much stronger than seen for T_g in figure 12 indicating that the condensation action of SSA is a more significant effect than their effect on ice nucleation. Thus the most intense TC eyewalls will contain the smallest droplets in comparison to their periphery clouds, implying increased aerosol presence in these clouds which is also consistent with the idealized case proposed by Shpund[22].

4 Conclusion

This investigation has shown using two distinct approaches that there is evidence for the presence of sea spray aerosol exclusively in the eyewall of intense TCs. The distribution of glaciation temperature T_g inside the eyewall indicates that there is a class of TCs with a T_g warmer than the homogeneous freezing temperature expected for high updraft convective clouds[33] and this peak is not seen when considering the clouds in the TC periphery. This therefore indicates the presence of aerosol exclusively present to the eyewall. In particular TCs of category 5 intensity were more likely to be present inside this peak indicating that the quantity of the aerosol may be dependent on the intensity of the TC.

Via a separate method of considering the composite profiles between the eyewall and periphery it was found that the $3.7\mu m$ reflectance in the eyewall is larger than that of the periphery for all temperatures showing that the particle size is consistently smaller in the eyewall as has been speculated by several previous studies of a more limited range of TCs[22, 24]. The difference in the rainout region of the profiles, where the giant CCN action of SSA is expected to cause a rapid increase in the precipitation and thus reduction in particle radius, was shown to be moderately correlated to the maximum wind speed of the TC. This is again consistent with previous expectations for SSA formation which will be increased for TCs with the highest wind speed.

This investigation has also showed that the high resolution of the VIIRS imaging band can offer a deep insight into the microphysical processes taking place in extreme environments such as the eyewall. The method developed by Yuan et al to estimate the glaciation temperature was also shown to work partially successfully in the eyewall and TC periphery. However there were still many TC images that were rejected from the catalogue wing to poor profile fits and un-physical glaciation temperatures. The quality of the fits could be improved by using a more advanced model of the evolution of particle size in the mixed-phase region as well as factoring in the evolution of particle sizes in the lower rainout and diffusion regions. In addition, this investigation was limited by the low number of total images present as using daytime images from VIIRS only provided 1 image per day of a given TC. Thus further refinement of this method to allow profiles to be determined at night would double the dataset of

potential images.

In conclusion, the results of this report agree with the previous suggestions on the effect of SSA in the eyewall, with a reduction in particle size in comparison to that in the TC periphery. In addition, a subset of the TC images also suggest that SSA are able to impact ice nucleation processes inside the eyewall resulting in the warmer than homogeneous glaciation temperature seen in just under half all investigated images. These observations demonstrate the importance of accounting for cloud microphysical processes in tropical cyclone simulations and could motivate further research into whether SSA are also able to trigger rapid intensification in tropical cyclones.

References

- [1] s Shaikh Eskander and Edward B. Barbier. *Long-Run Impacts of the 1970-74 Series of Disasters in Bangladesh*. SSRN Scholarly Paper ID 2548744. Rochester, NY: Social Science Research Network, Dec. 18, 2014. URL: <https://papers.ssrn.com/abstract=2548744>.
- [2] s MZ Hossain et al. "Impact of tropical cyclones on rural infrastructures in Bangladesh". In: *Agricultural Engineering International: CIGR Journal* (2008).
- [3] s Lixion A. Avila. "The 2018 Atlantic Hurricane Season: Another Catastrophic Year for the United States". In: *Weatherwise* 72.4 (July 4, 2019), pp. 14–21. ISSN: 0043-1672. DOI: 10.1080/00431672.2019.1612201. URL: <https://doi.org/10.1080/00431672.2019.1612201>.
- [4] s John Kaplan, Mark DeMaria, and John A. Knaff. "A Revised Tropical Cyclone Rapid Intensification Index for the Atlantic and Eastern North Pacific Basins". In: *Weather and Forecasting* 25.1 (Feb. 2010), pp. 220–241. ISSN: 0882-8156, 1520-0434. DOI: 10.1175/2009WAF2222280.1. URL: <http://journals.ametsoc.org/doi/abs/10.1175/2009WAF2222280.1>.
- [5] s Kerry Emanuel. "Tropical Cyclones". In: *Annual Review of Earth and Planetary Sciences* 31.1 (2003), pp. 75–104. DOI: 10.1146/annurev.earth.31.100901.141259. URL: <https://doi.org/10.1146/annurev.earth.31.100901.141259>.
- [6] s William M. Gray. "Global view of the origin of tropical disturbances and storms". In: *Monthly Weather Review* 96.10 (Oct. 1, 1968), pp. 669–700. ISSN: 0027-0644. DOI: 10.1175/1520-0493(1968)096<0669:GVOT00>2.0.CO;2. URL: <https://journals.ametsoc.org/doi/abs/10.1175/1520-0493%281968%29096%3C0669%3AGVOT00%3E2.0.CO%3B2>.
- [7] s Martin L. M. Wong and Johnny C. L. Chan. "Tropical Cyclone Intensity in Vertical Wind Shear". In: *Journal of the Atmospheric Sciences* 61.15 (Aug. 1, 2004), pp. 1859–1876. ISSN: 0022-4928. DOI: 10.1175/1520-0469(2004)061<1859:TCIIVW>2.0.CO;2. URL: <https://journals.ametsoc.org/doi/10.1175/1520-0469%282004%29061%3C1859%3ATCIIVW%3E2.0.CO%3B2>.
- [8] s Timothy Schott et al. *The Saffir-Simpson Hurricane Wind Scale*. Jan. 2, 2019. URL: <https://www.nhc.noaa.gov/pdf/sshws.pdf>.

- [9] s Daniel P. Stern, George H. Bryan, and Sim D. Aberson. "Extreme Low-Level Updrafts and Wind Speeds Measured by Dropsondes in Tropical Cyclones". In: *Monthly Weather Review* 144.6 (Apr. 1, 2016), pp. 2177–2204. ISSN: 0027-0644. DOI: 10.1175/MWR-D-15-0313.1. URL: <https://journals.ametsoc.org/doi/10.1175/MWR-D-15-0313.1>.
- [10] s Robert A. Houze. "Clouds in Tropical Cyclones". In: *Monthly Weather Review* 138.2 (Feb. 1, 2010), pp. 293–344. ISSN: 0027-0644. DOI: 10.1175/2009MWR2989.1. URL: <https://journals.ametsoc.org/doi/full/10.1175/2009MWR2989.1>.
- [11] s Daniel Rosenfeld and Itamar M. Lensky. "Satellite-Based Insights into Precipitation Formation Processes in Continental and Maritime Convective Clouds". In: *Bulletin of the American Meteorological Society* 79.11 (Nov. 1, 1998), pp. 2457–2476. ISSN: 0003-0007. DOI: 10.1175/1520-0477(1998)079<2457:SBIIPF>2.0.CO;2. URL: <https://journals.ametsoc.org/doi/abs/10.1175/1520-0477%281998%29079%3C2457%3ASBIIPF%3E2.0.CO%3B2>.
- [12] s James E. Hansen and Larry D. Travis. "Light scattering in planetary atmospheres". In: *Space Science Reviews* 16.4 (Oct. 1, 1974), pp. 527–610. ISSN: 1572-9672. DOI: 10.1007/BF00168069. URL: <https://doi.org/10.1007/BF00168069>.
- [13] s Teruyuki Nakajima and Michael D. King. "Determination of the Optical Thickness and Effective Particle Radius of Clouds from Reflected Solar Radiation Measurements. Part I: Theory". In: *Journal of the Atmospheric Sciences* 47.15 (Aug. 1, 1989), pp. 1878–1893. ISSN: 0022-4928. DOI: 10.1175/1520-0469(1990)047<1878:DOTOTA>2.0.CO;2. URL: <https://journals.ametsoc.org/doi/abs/10.1175/1520-0469%281990%29047%3C1878%3ADOTOTA%3E2.0.CO%3B2>.
- [14] s Daniel Rosenfeld and Garik Gutman. "Retrieving microphysical properties near the tops of potential rain clouds by multispectral analysis of AVHRR data". In: *Atmospheric Research*. 11th conference on clouds and precipitation 34.1 (June 20, 1994), pp. 259–283. ISSN: 0169-8095. DOI: 10.1016/0169-8095(94)90096-5. URL: <http://www.sciencedirect.com/science/article/pii/0169809594900965>.
- [15] s Tianle Yuan et al. "Estimating glaciation temperature of deep convective clouds with remote sensing data". In: *Geophysical Research Letters* 37.8 (2010). ISSN: 1944-8007. DOI: 10.1029/2010GL042753. URL: <https://agupubs.onlinelibrary.wiley.com/doi/abs/10.1029/2010GL042753>.
- [16] s Alexei Korolev. "Limitations of the Wegener–Bergeron–Findeisen Mechanism in the Evolution of Mixed-Phase Clouds". In: *Journal of the Atmospheric Sciences* 64.9 (Sept. 1, 2007), pp. 3372–3375. ISSN: 0022-4928. DOI: 10.1175/JAS4035.1. URL: <https://journals.ametsoc.org/doi/full/10.1175/jas4035.1>.
- [17] s Daniel Rosenfeld et al. "Glaciation temperatures of convective clouds ingesting desert dust, air pollution and smoke from forest fires". In: *Geophysical Research Letters* 38.21 (2011). ISSN: 1944-8007. DOI: 10.1029/2011GL049423. URL: <https://agupubs.onlinelibrary.wiley.com/doi/abs/10.1029/2011GL049423>.
- [18] s Henian Zhang et al. "Direct and indirect impacts of Saharan dust acting as cloud condensation nuclei on tropical cyclone eyewall development". In: *Geophysical Research Letters* 36.6 (2009). ISSN: 1944-8007. DOI: 10.1029/2009GL037276. URL: <https://agupubs.onlinelibrary.wiley.com/doi/abs/10.1029/2009GL037276>.

- [19] s Kerry A. Emanuel. “An Air-Sea Interaction Theory for Tropical Cyclones. Part I: Steady-State Maintenance”. In: *Journal of the Atmospheric Sciences* 43.6 (Mar. 1, 1986), pp. 585–605. ISSN: 0022-4928. DOI: 10.1175/1520-0469(1986)043<0585:AASITF>2.0.CO;2. URL: [https://journals.ametsoc.org/doi/abs/10.1175/1520-0469\(1986\)043%3C0585:AASITF%3E2.0.CO;2](https://journals.ametsoc.org/doi/abs/10.1175/1520-0469(1986)043%3C0585:AASITF%3E2.0.CO;2).
- [20] s M. A. Donelan. “On the limiting aerodynamic roughness of the ocean in very strong winds”. In: *Geophysical Research Letters* 31.18 (2004), p. L18306. ISSN: 0094-8276. DOI: 10.1029/2004GL019460. URL: <http://doi.wiley.com/10.1029/2004GL019460>.
- [21] s Mark D. Powell, Peter J. Vickery, and Timothy A. Reinhold. “Reduced drag coefficient for high wind speeds in tropical cyclones”. In: *Nature* 422.6929 (Mar. 2003), pp. 279–283. ISSN: 1476-4687. DOI: 10.1038/nature01481. URL: <https://www.nature.com/articles/nature01481>.
- [22] s J. Shpund, A. Khain, and D. Rosenfeld. “Effects of Sea Spray on the Dynamics and Microphysics of an Idealized Tropical Cyclone”. In: *Journal of the Atmospheric Sciences* 76.8 (Aug. 2019), pp. 2213–2234. ISSN: 0022-4928, 1520-0469. DOI: 10.1175/JAS-D-18-0270.1. URL: <http://journals.ametsoc.org/doi/10.1175/JAS-D-18-0270.1>.
- [23] s Baolin Jiang et al. “Simulation of the effects of sea-salt aerosols on cloud ice and precipitation of a tropical cyclone”. In: *Atmospheric Science Letters* 20.9 (Sept. 2019). ISSN: 1530-261X, 1530-261X. DOI: 10.1002/asl.936. URL: <https://onlinelibrary.wiley.com/doi/abs/10.1002/asl.936>.
- [24] s Jinya John et al. “Study of satellite-derived cloud microphysical parameters for tropical cyclones over the North Indian Ocean (2010–2013)”. In: *Theoretical and Applied Climatology* 139.3 (Feb. 1, 2020), pp. 1163–1173. ISSN: 1434-4483. DOI: 10.1007/s00704-019-03047-9. URL: <https://doi.org/10.1007/s00704-019-03047-9>.
- [25] s VIIRS/NPP Imagery Resolution 6-Min L1B Swath 375m. In collab. with VCST Team. 2016. URL: <https://modaps.modaps.eosdis.nasa.gov/services/about/products/viirs-c1/VNP02IMG.html>.
- [26] s Changyong Cao et al. *Visible Infrared Imaging Radiometer Suite (VIIRS) Sensor Data Record (SDR) User’s Guide*. Mar. 2, 2017. URL: <https://ncc.nesdis.noaa.gov/documents/documentation/viirs-users-guide-tech-report-142a-v1.3.pdf>.
- [27] s D. Rosenfeld et al. “High-resolution (375 m) cloud microstructure as seen from the NPP/VIIRS satellite imager”. In: *Atmospheric Chemistry and Physics* 14.5 (Mar. 10, 2014), pp. 2479–2496. ISSN: 1680-7316. DOI: <https://doi.org/10.5194/acp-14-2479-2014>. URL: <https://www.atmos-chem-phys.net/14/2479/2014/>.
- [28] s Zhiguo Yue et al. “Automated Mapping of Convective Clouds (AMCC) Thermodynamical, Microphysical, and CCN Properties from SNPP/VIIRS Satellite Data”. In: *Journal of Applied Meteorology and Climatology* 58.4 (Feb. 12, 2019), pp. 887–902. ISSN: 1558-8424. DOI: 10.1175/JAMC-D-18-0144.1. URL: <https://journals.ametsoc.org/doi/10.1175/JAMC-D-18-0144.1>.
- [29] s Martin Raspaud et al. “PyTroll: An Open-Source, Community-Driven Python Framework to Process Earth Observation Satellite Data”. In: *Bulletin of the American Meteorological Society* 99.7 (May 9, 2018), pp. 1329–1336. ISSN: 0003-0007. DOI: 10.1175/BAMS-D-17-0277.1. URL: <https://journals.ametsoc.org/doi/full/10.1175/BAMS-D-17-0277.1>.

- [30] s Kenneth R. Knapp et al. “The International Best Track Archive for Climate Stewardship (IBTrACS)”. In: *Bulletin of the American Meteorological Society* 91.3 (Mar. 1, 2010), pp. 363–376. ISSN: 0003-0007. DOI: 10.1175/2009BAMS2755.1. URL: <https://journals.ametsoc.org/doi/abs/10.1175/2009BAMS2755.1>.
- [31] s Toshiro Inoue. “An Instantaneous Delineation of Convective Rainfall Areas Using Split Window Data of NOAA-7 AVHRR”. In: *Journal of the Meteorological Society of Japan. Ser. II* 65.3 (1987), pp. 469–481. ISSN: 0026-1165, 2186-9057. DOI: 10.2151/jmsj1965.65.3_469. URL: https://www.jstage.jst.go.jp/article/jmsj1965/65/3/65_3_469/_article.
- [32] s I. M. Lensky and D. Rosenfeld. “The time-space exchangeability of satellite retrieved relations between cloud top temperature and particle effective radius”. In: *Atmospheric Chemistry and Physics* 6.10 (July 12, 2006), pp. 2887–2894. ISSN: 1680-7316. DOI: <https://doi.org/10.5194/acp-6-2887-2006>. URL: <https://www.atmos-chem-phys.net/6/2887/2006/>.
- [33] s Alexei Korolev and George Isaac. “Phase transformation of mixed-phase clouds”. In: *Quarterly Journal of the Royal Meteorological Society* 129.587 (2003), pp. 19–38. ISSN: 1477-870X. DOI: 10.1256/qj.01.203. URL: <https://rmets.onlinelibrary.wiley.com/doi/abs/10.1256/qj.01.203>.